The role of metallic and acid sites of Ru-Nb-Si catalysts in the transformation of levulinic acid to γ-valerolactone

Serena Esposito [a], Brigida Silvestri [b], Carmelina Rossano [c], Valeria Vermile [c,d], Claudio Imparato [b], Maela Manzoli [e], Barbara Bonelli [a], Vincenzo Russo [c], Eric M. Gaigneaux [d], Antonio Aronne [b,*], Martino Di Serio [c,*]

[a] *Department of Applied Science and Technology and INSTM Unit, Politecnico di Torino, Corso Duca degli Abruzzi 24, IT-10129 Turin, Italy*
[b] *Department of Chemical, Materials and Production Engineering, University of Naples Federico II, Piazzale Tecchio 80, IT-80125 Naples, Italy*
[c] *Department of Chemical Sciences, University of Naples Federico II, Via Cinthia, IT-80126 Naples, Italy*
[d] *Université Catholique de Louvain, Institute of Condensed Matter and Nanosciences (IMCN), Place Louis Pasteur 1. L04.01.09, BE-1348 Louvain-la-Neuve, Belgium*
[e] *Department of Drug Science and Technology and NIS, Interdepartmental Centre, University of Turin, Via Pietro Giuria 9, 10125 Turin, Italy*

ARTICLE INFO

ABSTRACT

The transformation of γ-valerolactone (GVL) into levulinic acid (LA) requires the use of bifunctional catalysts allowing the hydrogenation and lactonization steps to occur. The aim of this study is to clarify the role played by both redox (Ru) and acid (Nb) sites of the ruthenium-niobium-silicon mixed oxides catalysts, synthesized by sol-gel route, when this reaction is performed in mild conditions. The catalytic performances of the materials are related to an in-depth morphologic and structural characterization, demonstrating that the interaction between the two metals and their relative amount and dispersion are crucial in determining their activity. The results confirm the hydrogenation-dehydration consecutive reaction network and evidence the possibility to selectively produce either GVL or the intermediate γ-hydroxypentanoic acid by an accurate choice of the catalyst composition.

1. Introduction

The enormous potential of the biomass conversion into value added products is a key point to ease the pressure on the global crisis about fossil resources and to reduce the environmental pollution.

Biomass, through the photosynthesis process, absorbs water, sunlight and the available atmospheric CO_2, which is then released during the combustion process realizing what is called "closed carbon cycle", with net zero emissions that do not contribute to the global warming [1, 2]. Furthermore, biomass and biomass derived compounds are relatively cheap, and they are ethically accepted by the society because their production does not compete with food crop production. The research community based on this motivation is looking for the development of new and economically viable routes to sustainable chemical products.

In this context, many studies have highlighted the lignocellulosic biomass as feedstock to obtain levulinic acid (LA), that was identified by the United States Department of Energy as key target molecule for the production of renewable fuels, fuel additives, green solvents, polymers, value-added fine chemicals, flavoring agents and resins [3–6].

Thus, LA offers one of the largest families of derivatives of potential industrial interest because it possesses both keto and carboxylic acid groups and with this special molecular structure a series of chemical reactions such as esterification, hydrogenation, halogenation, and oxidation can occur. To highlight the value of LA, the most promising reaction is the hydrogenation to γ-valerolactone (GVL), a platform molecule that has gained considerable attention in the last decade.

GVL is a heterocyclic five carbon ester ($C_5H_8O_2$) with one methyl group in γ-position, has a sweet, herbaceous odor that makes it perfect for application in perfumes and food additives [7,8]. For its attractive physicochemical properties, GVL can be used as a solvent for various processes, for the synthesis of biomass derived chemicals; a precursor for even higher value-added chemicals (like 1,4-pentanediol, 2-methyletrahydrofuran) and in the fuel sector [9–11].

Although GVL also possesses a stereogenic carbon center, the major applications in the fuel sector or as solvent does not require a specific enantiomeric form and GVL is usually synthesized and used in the

racemic form.

According to the literature, the production of GVL from LA hydrogenation over a catalyst is the most efficient and economic method reported to date [12]. Both homogeneous and heterogeneous catalysts have been studied over the past decades for this reaction. Typically, precious metals such as iridium (Ir) [13], palladium (Pd) [14], platinum (Pt) [15] and ruthenium (Ru) [16,17] are the most often used catalysts. In particular, Ru-based catalysts are by now classified as benchmark catalysts for this reaction, since high GVL yield can be reached ($> 97\%$) under relatively mild condition [18].

The most accredited reaction pathway at low temperature is the hydrogenation of LA to γ-hydroxypentanoic acid (HPA) followed by the intramolecular lactonization to GVL [19,20].

A recent mechanistic study performed by isotopic labeling experiments has confirmed the above hypotheses establishing that the hydrogenation goes mainly via HPA and subsequent lactonization when the reaction occurs in mild conditions using Ru/C as catalyst [21].

It has been hypothesized that the two reactions are catalyzed by two different sites: the metallic sites for hydrogenation reaction and the acid sites for the lactonization reaction. Although Ru/C is the commonly used catalyst for such reaction, being characterized by the presence of both metallic and acid sites, [22] it suffers from slow but irreversible deactivation, probably due to the sintering of the ruthenium particles and the formation of carbonaceous deposits on the catalyst surface.

Lately we have synthesized a bifunctional catalyst, obtained by a proper reduction of a gel-derived $(RuO_2)_{0.038}(Nb_2O_5)_{0.024}(SiO_2)_{0.938}$ nanomaterial, showing a much higher stability than Ru/C catalysts for this reaction and characterized by a high and uniform dispersion of Ru nanoparticles in the acid matrix [20]. In particular, the mentioned catalyst showed an activity of 370 times higher than Ru/C, considered nowadays a benchmark catalyst for γ-valerolactone synthesis activity [20].

In a recent review Yu et al. [23] examined the effects of the acid characteristic of the support in which the metallic phase is dispersed on the performance of bifunctional catalysts for the heterogeneous transformation LA to GVL. They conclude that the acidity of the support plays a key role in this transformation affecting both the metal dispersion and the stability of the catalyst in mild reaction conditions [23].

In this paper the effect of the chemical composition of different Ru-Nb-Si gel-derived nanostructured materials on the catalytic performance in the LA hydrogenation reaction was explored with special attention to the acid surface characteristics of the matrix in which the Ru nanoparticles are dispersed. Keeping the RuO_2 amount at 3.8 mol% the Nb_2O_5 content was changed from 0 to 6.9 mol% in the RuO_2-Nb_2O_5-SiO_2 (Ru-Nb-Si) mixed-oxide system with the aim to clarify the role played by the two components (the metallic phase and the acid matrix) in determining the reaction pathway and then the GVL yields. In this context, the possibility to study the interaction between Ru and Nb is of pivotal importance. Therefore, Field Emission Scanning Electron Microscopy (FESEM) combined with Energy Dispersive Spectroscopy (EDS) mapping were employed to get information at nanometric level on the location of the Ru and Nb metals within the silica matrix, depending on the composition of the catalysts. This advanced tridimensional characterization allowed therefore to monitor the morphology and to make correlations with the composition close to the surface of the materials upon activation. It should be noted that modulating the composition of the support and then its acid characteristics, either HPA or GVL were isolated as the only product of the reaction.

2. Materials and methods

2.1. Sol-gel synthesis

The following reagents by Sigma–Aldrich were used: tetraethoxysilane (TEOS, Si(OC$_2$H$_5$)$_4$ 99%), niobium(V) chloride, (NbCl$_5$ 99%), ruthenium(III) chloride-3-hydrate (RuCl$_3$.3 H$_2$O 99.98%), anhydrous

Table 1
Composition and textural properties of studied samples.

Sample	Molar Composition	N$_2$ physisorption[a]	NH$_3$-TPD[a]	Nb/Ru[b]		D$_{Ru}$[c]
		S$_{BET}$[d] (m^2 g^{-1})	Acid sites[e] (mmol/g)	Ox[a]	Red[f]	
4Ru0Nb	RuO$_2$ (0.038)·SiO$_2$ (0.962)	523[g]	> 0.01	–	–	12
4Ru 2.5 Nb	RuO$_2$ (0.038)·Nb$_2$O$_5$ (0.024)·SiO$_2$ (0.938)	398	0.72	0.6	1.6	5
4Ru5Nb	RuO$_2$ (0.038)·Nb$_2$O$_5$ (0.047)·SiO$_2$ (0.915)	472	0.51	1.1	3.6	5
4Ru 7.5 Nb	RuO$_2$ (0.038)·Nb$_2$O$_5$ (0.069)·SiO$_2$ (0.893)	412	0.47	1.9	11.0	4

[a] annealed sample at 500 °C for 2 h.
[b] Nb/Ru mass ratio of Nb and Ru average amounts from EDS maps of different regions of the sample.
[c] ruthenium dispersion obtained by CO chemisorption.
[d] specific surface area calculated by BET method.
[e] amount of NH$_3$ chemisorbed per gram of sample.
[f] reduced sample in H$_2$ (1 bar, 0.1 mL/min) at 300 °C for 3 h.
[g] [24].

ethanol (EtOH). Mixed-oxide materials, whose nominal molar composition is reported in Table 1, were prepared by a one-pot sol-gel route with slight modification of our previous procedure [20].

More in detail, an alcoholic solution of NbCl$_5$ with a molar ratio NbCl$_5$/EtOH = 1:6 was prepared in a dry box at room temperature. The solution was stirred for 60 min to allow the formation of partially substituted Nb(OEt)$_{5-x}$(Cl)$_x$ species and the removal of produced HCl. To an alcoholic solution of TEOS (with molar ratio TEOS/EtOH = 1:4) a proper amount of RuCl$_3$.3 H$_2$O was added and the latter solution was mixed with the former. The resulting clear reddish mixture was hydrolyzed at room temperature by using deionized water (with final molar ratio TEOS/H$_2$O = 1:4). Transparent dark-red gels were obtained within few days, depending on the Nb content; the gelled systems were kept aging for 3 days and then fully dried in air at 110 °C in an electric oven. The amorphous dried gels (xerogels) were annealed for 2 h at 500 °C in air (Table 1).

The catalysts used in the reaction were obtained from these materials by a reduction treatment under a 0.1 L min^{-1} H$_2$ flow, 1 bar, 300 °C for 3 h and finally cooled at room temperature (r.t.) under H$_2$ flow.

2.2. Structural, morphological, and surface acidity characterization

X-ray diffraction patterns were recorded with a Bruker D8 X-ray diffractometer, operating in the reflection mode with Cu-Kα radiation (λ = 1.5418 Å, 40 kV, 30 mA). The data were collected in the 5–80° range (2θB) with steps of 0.015°, time per step of 0.15 s

FTIR (Fourier Transform Infrared) spectra were collected in the ATR (Attenuated Total Reflection) mode using a Bruker Equinox 55 spectrometer equipped with a Platinum ATR cell, in which diamond (refractive index = 2.41) is used as ATR crystal. The spectra were recorded with 100 scans between 4000 and 500 cm^{-1} with a resolution of 4 cm^{-1}.

DR UV–vis (Diffuse Reflectance UV-Visible) spectra were recorded in the range of 200 – 800 nm on a Shimadzu UV-3600 Plus spectrophotometer. A Spectralon® Diffuse Reflectance Standard was used to

measure the background spectra. The measured intensity was expressed as the value of the Kubelka–Munk function F(R).

N$_2$ adsorption/desorption isotherms at −196 °C were obtained with a QuantachromeAutosorb 1 instrument on samples previously outgassed at 300 °C under vacuum for 3 h to remove water and other atmospheric contaminants. The BET (Brunauer-Emmett-Teller) method was used to calculate the samples specific surface area, *SBET*.

FTIR spectroscopy measurements of NH$_3$ adsorption were carried out at room temperature (r.t.). FTIR spectra of self-supporting wafers were collected on an Equinox 55 (Bruker) spectrophotometer equipped with MCT (Mercury – Cadmium- Telluride) cryodetector. The powders were pressed into thin self-supporting wafers (optical density of about 20 mg cm^{-2}) and treated under high vacuum (residual pressure <10^{-3} mbar) at 300 °C in a standard vacuum frame, to remove water and other atmospheric contaminants. Afterwards, increasing pressures of NH$_{3(g)}$ were dosed on the outgassed samples (equilibrium pressure range: 0–15 mbar) and then, the samples were outgassed for 1 h at r.t. and at 300 °C, to check adsorption reversibility.

NH$_3$-TPD (Temperature Programmed Desorption) measurements were carried out using a CATLAB-PCS (Hiden Analytical), a quartz microreactor coupled to a Mass Spectrometer. About 0.1 g fresh sample was preheated in argon flow (50 mL min^{-1}) at 300 °C for 60 min (ramp 10 °C min^{-1}). Adsorption of NH$_3$ (5 vol% in helium; flow rate 30 mL min^{-1}) was done at 70 °C. The TPD measurement, under an argon flow of 30 mL min^{-1}, was conducted by heating the sample from 70° to 600°C at a 10 °C min^{-1} rate.

FESEM (Field Emission Scanning Electron) measurements were performed using a Tescan S9000G FESEM 3010 microscope (30 kV) equipped with a high brightness Schottky emitter and fitted with Energy Dispersive X-ray Spectroscopy (EDS) analysis by an Ultim Max Silicon Drift Detector (SDD, Oxford). For analyses, the samples, in the form of powders, were deposited on a stub coated with a conducting adhesive and inserted in the chamber by a fully motorized procedure. In order to determine the Nb/Ru ratios listed in Table 1 for 4Ru 2.5 Nb, 4Ru5Nb and 4Ru 7.5 Nb, EDS mapping were carried out on each sample either annealed for 2 h at 500 °C in air or successively reduced for 3 h at 300 °C under H$_2$ flow. The EDS analyses were performed on different regions of each sample by adopting the same instrumental beam parameters to keep constant the interaction volume. In this way, the average amounts (weight %) of Nb and Ru were obtained and then the Nb/Ru ratios were calculated.

XPS (X-ray Photoelectron Spectroscopy) analysis was carried out on an XPS PHI 5000 Versa probe apparatus, using a band-pass energy of 187.85 eV, a 45° take off angle and a 100.0 μm diameter X-ray spot size for survey spectra. High-resolution XP spectra were recorded in the following conditions: pass energy of 20 eV, resolution of 0.1 eV and step of 0.2 eV. Sample charging effects were eliminated by referring to the spectral line shift of the C 1 s binding energy (BE) value at 284.8 eV. XP-spectra were analysed by means of a commercial software (CasaXPS, version 2.3.16).

Carbon monoxide chemisorption was performed in a Micromeritics Pulse Chemisorb 2705 equipment. The catalyst (0.15 g), placed in a U-shaped sample tube, was heated at a rate of 10 °C min^{-1}, under a pure flow of H$_2$, to perform a reduction pretreatment at 300 °C for 3 h. The sample was cooled down to 35 °C. The CO chemisorption was performed sending pulses of 0.037 mL of CO in helium, to the sample and recording the corresponding peak value of the non adsorbed CO. This process was repeated until saturation, namely when no more CO was adsorbed when an additional pulse is given. The total amount of CO adsorbed is found by summing the amount adsorbed at each pulse.

2.3. Catalytic tests

The catalytic experiments were conducted following our previous studies in the field [20]. The experimental procedure is here briefly described: 4.0 g of LA, 200 g of water and 0.5 g of pre-reduced catalyst
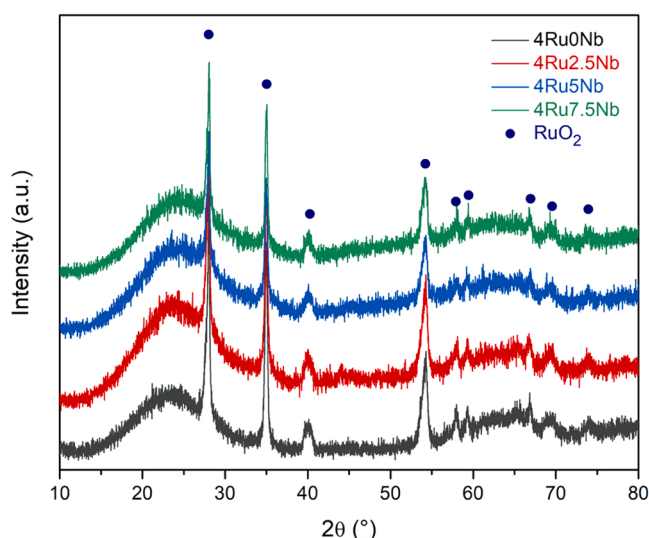

Fig. 1. XRD patterns of gel-derived materials annealed at 500 °C for 2 h. The pattern of the corresponding 4Ru0Nb sample is also reported as a reference.

were loaded to the reactor. The system was heated at 70 °C at a constant stirring rate of 300 rpm, then hydrogen was fed at a constant pressure. Samples were withdrawal along the experimental time to measure the products distribution via GC analysis, using ethylene glycol as an external standard (100 μL in 2 mL of reaction sample). The sample (1 μL) was injected in a PerkinElmer Clarus 580 GC, working with a 30 m x 0.32 mm× 0.26 μm Supelco SLB-IL60 column, with a FID detector, a PSSI injector working at 300 °C, carrier (He) pressure of 14 psi and working in on-column mode. The temperature ramp was set as follows: 100 °C heating to 300 °C with a rate of 10 °C min^{-1}; the temperature was kept at the final value for 25 min. The retention times were the following: ethylene glycol: 4.7 min; γ-valerolactone: 6.2 min; γ-hydroxypentanoic acid: 7.11 min; levulinic acid: 10.4 min

The reliability of GC-FID analysis was checked by comparing the results with the ones obtained via ^{1}H NMR: GVL and HPA selectivity values show an error below 6% (see Supplementary Material).

The catalyst pre-treatment was performed in a fixed bed reactor working at 0.1 L min^{-1} H$_2$ flow, 1 bar and 300 °C for 3 h.

3. Results and discussion

3.1. Structural, textural, and electronic properties

All dried gels are amorphous (data not shown) while the XRD profiles of the annealed samples (2 h at 500 °C) are shown in Fig. 1. The peaks of Ru(IV) oxide, RuO$_2$, (JCPDS Card No. 40–1290) can be noticed in all profiles [20,25] together with a broad halo centered at approximately 2θ = 24°, typical of amorphous silica [26–28]. This indicates that the annealing causes the precipitation in the amorphous matrix of small RuO$_2$ crystals.

On the other hand, the lack of typical peaks of Nb$_2$O$_5$ crystalline aggregates corroborates the hypothesis of a very high dispersion of niobium in the siloxane matrix. Actually, the highest lines for the monoclinic (H-Nb$_2$O$_5$, JCPDS card 32–711) and the orthorhombic (T-Nb$_2$O$_5$, JCPDS card 27–1312) polymorphs occur in the 20°–25° 2θ range where only the peak of the amorphous halo is seen (Fig. 1). On the other hand, due to the more complex structure of H-phase, containing 3 × 5 and 3 × 4 ReO$_3$ type blocks superstructures, than the T-phase one, formed by corner- and edge- sharing distorted octahedra and pentagonal bipyramids, it was expected that at this temperature the initial crystallization of T-Nb$_2$O$_5$ could eventually occur at least for the samples at high Nb content, but the bottom-up procedure adopted to synthesize the materials allow to obtain a dispersion of niobium into the siloxane

matrix at molecular level, as demonstrated by the structural characterization later on reported [29].

The FTIR-ATR spectra of the annealed samples are displayed in Fig. S1. In the range 2850–3650 cm^{-1}, the FTIR-ATR spectra of all the samples exhibit a broad absorption band due to the O-H stretching mode of H-bonded hydroxy groups, due to the adsorption of water vapor after exposure to the atmosphere, as the spectra were taken at ambient conditions. Accordingly, at lower wavenumbers (Fig. S1), the bending mode of adsorbed molecular water (δ_{O-H}) [30,31] is observed at 1630 cm^{-1}. All the samples show the typical vibration modes of siloxanes (Si-O-Si) groups in the silica network at 1055 and 1200 cm^{-1} and at 795 cm^{-1} assigned to the asymmetric (ν_{Si-O}) [32] and symmetric ($\nu_{Si-O-Si}$) [29] stretching mode of Si-O-Si groups. The spectrum of the 4Ru0Nb sample shows a band at 970 cm^{-1}, due to the stretching mode of Si-O-Ru groups, forming by insertion of Ru in the silica matrix [33]. Interestingly, the addition of Nb (samples 4Ru 2.5 Nb, 4Ru5Nb and 4Ru 7.5 Nb) brings about the appearance of a (more intense) absorption at much lower wavenumbers, i.e. 950 cm^{-1}, due to the progressive formation of Si—O—Nb bonds due to the insertion of Nb within the silica matrix [29], in agreement with the XRD findings.

The DR UV–vis spectra (Fig. S2) of the annealed samples containing niobium are dominated by the band due to the charge-transfer transition (from O^{2-} to Nb^{5+}) centered at about 245 nm. It can be assigned to distorted NbO$_6$ octahedra, which are associated with Brønsted acid sites.

As the niobium content increases, the peaks position shift to slightly higher wavelengths and the absorption bands become a little wider indicating the presence of a broad distribution of isolated NbO$_6$ octahedra (less or more distorted), in agreement with FESEM findings [34]. The lack of absorption bands above 300 nm suggests that the occurrence of niobia-like domains can be excluded since Nb$_2$O$_5$ strongly absorbs below 400 nm [35].

The specific surface areas were obtained by the elaboration of the N$_2$ adsorption isotherm using the BET method and reported in Table 1. The shape of the adsorption–desorption isotherms (not reported) appears of type Ib according to the IUPAC classification, indicating the possible presence of wide micropores; differently from a microporous material the plateau starts at P/P^0 > 0.2 values, suggesting the presence of a certain mesoporosity. According to the results, among the samples with the same content of ruthenium, the 4Ru0Nb catalyst displays the highest specific surface area (523 m^{2}g^{-1}) while a decrease can be observed in the samples containing niobium.

3.2. Surface acidity properties

The surface acidic properties of the synthesized materials were analysed by NH$_3$ temperature-programmed desorption (TPD) experiments (Fig. S3), the values of total amount of desorbed NH$_3$ being reported in Table 1. As expected, the 4Ru0Nb samples showed a negligible amount of desorbed NH$_3$, in agreement with the absence of Nb-related acidic species, the only acidic species being surface Si-OH groups interacting with NH$_3$ by H-bonding. The TPD curves of the Nb-containing samples showed, instead, two main desorption ranges: the former (at lower temperature) is due to the occurrence of weaker acidic sites (likely, Nb-related OH groups that act as Brønsted-Lowry sites forming NH$_4^+$ species upon interaction with NH$_3$), the latter (at higher temperature) is due to the occurrence of stronger acidic sites (i.e. Nb-related Lewis sites). The total amount of desorbed NH$_3$ (Table 1) is maximum with the 4Ru 2.5 Nb sample, and decreases with the 4Ru5Nb sample, which, in turn, shows a desorbed amount of NH$_3$ slightly higher than the 4Ru 7.5 Nb sample. Besides these quantitative aspects, an inspection of the TPD curves shows that by increasing the amount of Nb$_2$O$_5$ from 2.5 to 5 mol%, the amount of weaker Brønsted-Lowry sites decreases markedly and that of stronger Lewis acidic sites increases slightly. As a whole, weak Brønsted-Lowry sites are more abundant with the 4Ru 2.5 Nb sample, whereas strong sites are more abundant with the 4Ru5Nb sample. The 4Ru 7.5 Nb samples has less abundant sites of both
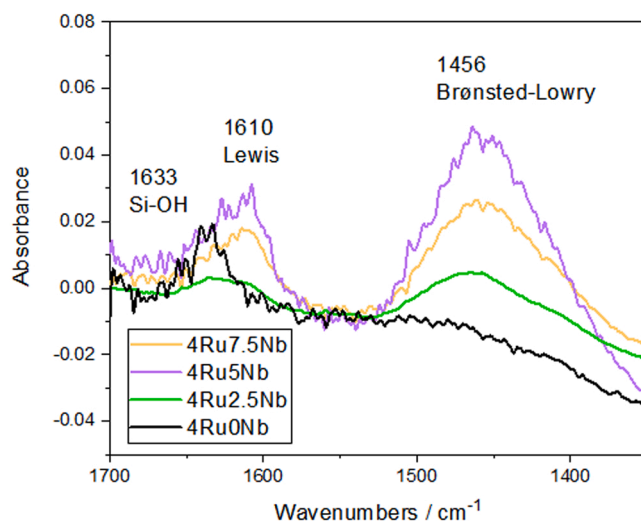

Fig. 2. Difference FTIR spectra concerning the room temperature adsorption of NH$_3$ (equilibrium partial pressure ca 5.0 mbar) on the samples previously outgassed at 300 °C. Spectra have been normalized to sample unit weight, in order to allow comparison.

types. The decrease of the acidity with the Nb content increase was also observed in the Nb-P-Si system where it was related to a higher cross-linking degree of Nb-O-Si and a consequent decrease of the fraction of isolated NbO$_4$ tetrahedra, which give a strong Lewis acidity, in agreement with DR UV–vis findings [36].

NH$_3$ TPD provided a quantitative aspect, i.e. the overall amount of sites. To qualitatively assess the nature of the acid sites at the surface of the synthesized materials, the adsorption of NH$_3$ was followed at r.t. by IR spectroscopy, since the protonated species (NH$_4^+$ ions) and the coordinatively bonded NH$_3$ in Lewis adducts have different N-H vibrations [37], and the small size of NH$_3$ allows probing of almost all acid sites in micro-, meso-, and macro-porous oxides [38]. In particular, the deformation vibrations (bending modes) at ca. 1450 and 1610–1630 cm^{-1} provide reliable indicators for the presence of protonated and coordinatively bonded NH$_3$, respectively. Fig. 2 reports difference spectra (after subtraction of the spectra of the bare samples, i.e., outgassed at 300 °C) taken after dosing ca. 20 mbar NH$_3$ at r.t. on the previously outgassed samples and, then, by decreasing the partial pressure to ca. 5.0 mbar NH$_{3(g)}$: the observed bands refer, therefore, to the species still adsorbed at the surface.

The analysis of the spectra in Fig. 2 reveals that, in the absence of Nb (4Ru0Nb sample), a single band is observed at 1633 cm^{-1}, readily ascribed to NH$_3$ molecules interacting with surface Si-OH species via H-bond [39,40], such OH groups being weakly acidic and, thus, unable to transfer a proton to NH$_3$, but able to H-bond the molecule at r.t.

As expected, the addition of Nb brings about the appearance of other two bands at ca. 1610 and 1456–1465 cm^{-1}. The former is assigned to the bending mode of NH$_3$ molecules adsorbed on coordinatively unsaturated Lewis sites (e.g. Nb^{5+} ions) [41], the latter to the bending mode of NH$_4^+$ species, formed upon interaction between NH$_3$ and Nb-related acidic -OH groups acting as Brønsted-Lowry sites. Such bands were not removed by prolonged evacuation at r.t., but by outgassing the samples at 300 °C (spectra not shown). Since the spectra have been normalized to sample unit weight, a comparison of the relative intensity of the bands is allowed, showing that with the 4Ru 2.5 Nb sample, which contains more abundant weaker sites, according to the TPD results, the bands are less intense and, moreover, the band due to the bending mode of the NH$_4^+$ species is seen at 1465 cm^{-1}, i.e., at lower wavenumbers than with the other two samples (4Ru5Nb and 4Ru 7.5 Nb), giving rise to a bending mode at 1456 cm^{-1}. The position of the bending mode is related to the strength of the interaction of NH$_3$ with surface OH groups, i.e., to their acidic strength [41] showing that the 4Ru 2.5 Nb has weaker
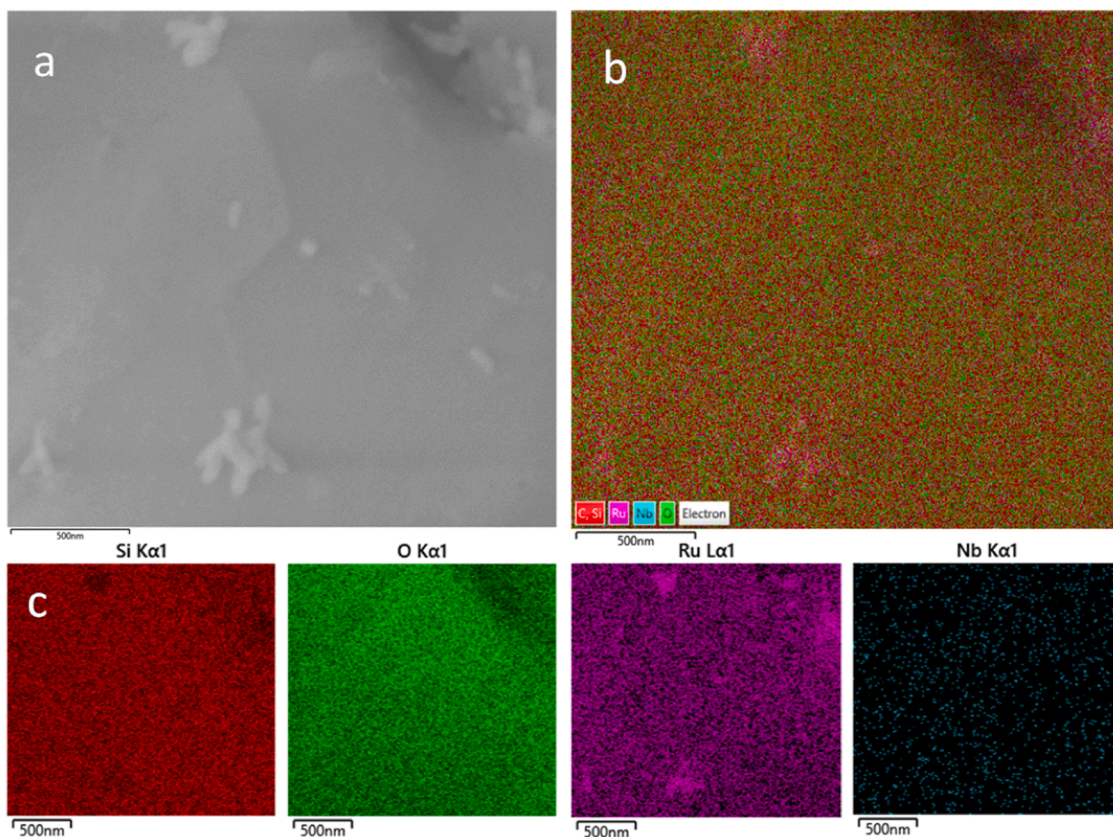
Fig. 3. FESEM image (a) and EDS layered image (b) of the 4Ru 2.5 Nb catalyst. EDS maps of the region shown in (a) for Si, O, Ru and Nb (c). Image collected at 25 kV with the standard SE detector. Instrumental magnification: 34,000x.

Brønsted-Lowry sites and less abundant Lewis sites, in agreement with the TPD results. Concerning the other two Nb-containing samples, the 4Ru5Nb catalysts seems to be the one containing more abundant stronger acidic sites, of both Lewis type and Brønsted-Lowry type and indeed in the TPD curve the component at ca. 250 °C is clearly observed, whereas at higher Nb loadings (4Ru 7.5 Nb) an overall decrease of acidity occurs likely due to some aggregation and, thus, lower accessibility of the Nb species.

3.3. Morphology and elemental distribution of both annealed and reduced materials

The morphology and element distribution of both annealed (500 °C in air for 2 h) and reduced (300 °C under H_2 flow for 3 h) materials were
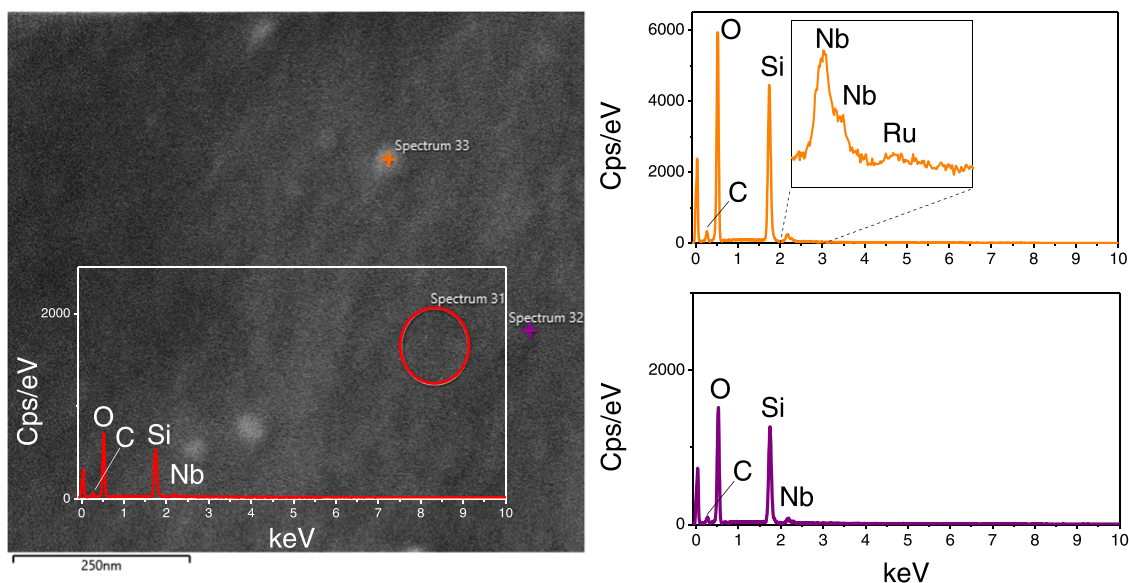

Fig. 4. FESEM representative image of 4Ru 2.5 Nb catalyst and EDS spectra of selected points/regions. Image collected at 25 kV with the standard SE detector. Instrumental magnification: 261,000x.
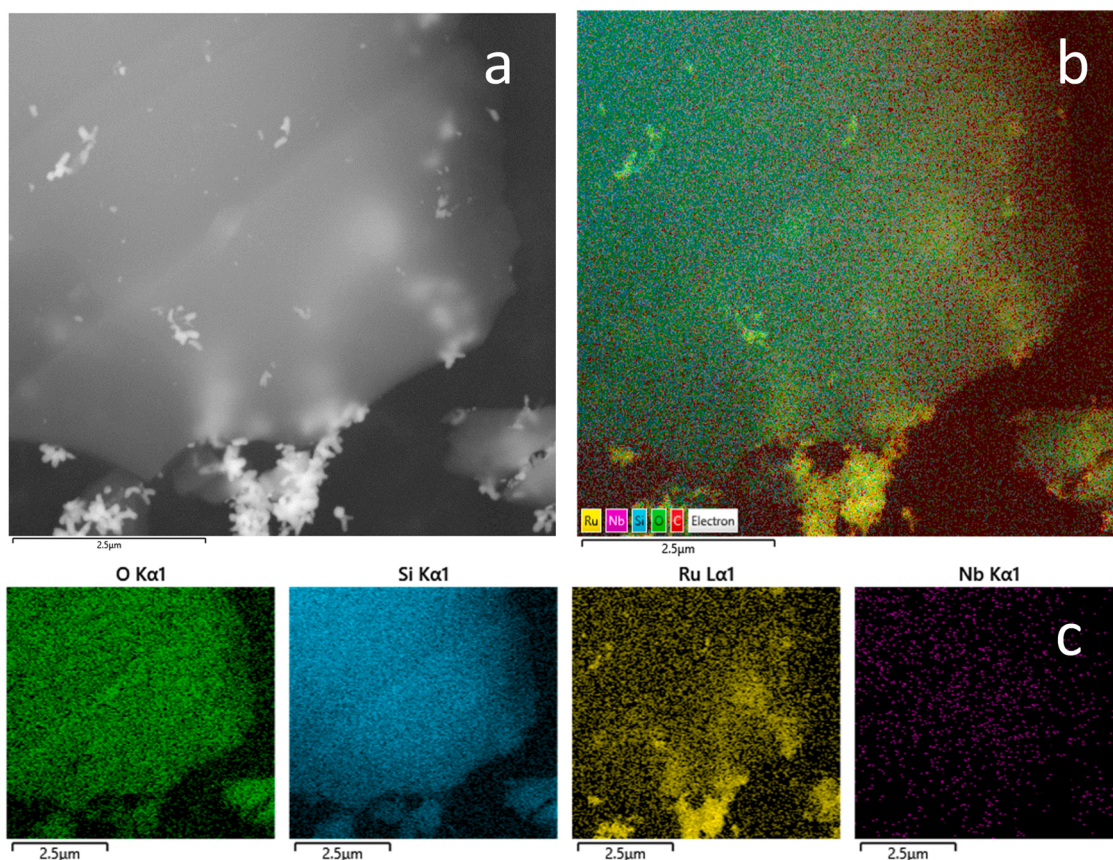
Fig. 5. FESEM image of the 4Ru5Nb catalyst (a), EDS layered image (b) with the corresponding EDS maps O, Si, Ru and Nb (c). Image collected at 25 kV with the standard SE detector. Instrumental magnification: 30,000x.

investigated by FESEM. The aim was to obtain information on the dispersion of Ru and Nb as well as on their respective arrangements within the materials to disclose the interaction between the two elements. Upon reduction at 300 °C the 4Ru0Nb catalyst contains large metallic Ru flower-like agglomerates, as shown in panel a of Fig. S4. Such peculiar Ru morphology was previously observed on the same sample annealed in air, before reduction (see Supplementary Material, Figs. S5 and S6) [24], confirming that the Ru flower-like morphology is not induced by the reduction treatment. Moreover, EDS analyses carried out on different points of the reduced sample (panel b of Fig. S4) clearly put in evidence the presence of Ru also in regions of the catalyst where the flower-like Ru species are not observed, therefore indicating that Ru species are homogeneously dispersed within the silica matrix, in agreement with the results of EDS mapping carried out on the annealed sample (panel c of Fig. S6) [20,27].

FESEM representative images of the 4Ru 2.5 Nb catalyst (reduced sample) are shown in panels a and b of Fig. 3, revealing similar Ru flower-like morphology also in the presence of Nb. EDS maps of Si, O, Ru and Nb showed homogeneous distribution of the different elements at nanometric scale within the 4Ru 2.5 Nb catalyst, panel c of Fig. 3 (additional experimental findings on both annealed and reduced materials are reported in Figs. S7–S9 of the Supplementary Material).

These findings were corroborated by measurements carried out at higher magnification (Fig. 4), that highlighted the Nb dispersion at atomic level, whereas Ru is in the form of very small nanoparticles with size similar to that observed previously for 4Ru0Nb [20,27]. These features put in evidence a close contact between the highly dispersed Nb and Ru species.

Morphology and element distribution were checked also in the case of both annealed and reduced 4Ru5Nb and 4Ru 7.5 Nb samples. Similar features were observed, as shown in Figs. 5 and 6, confirming that also in

these cases, Ru is located in regions where the flower-like morphology is not present and that Nb is homogeneously dispersed within the materials, independently of the Ru amount in the catalysts. (Further experimental evidence is reported in Figs. S10–S14 of the Supplementary Material.).

In Table 1 the Nb/Ru ratios calculated based on EDS maps (obtained as wt% of the different elements) are summarized for all ternary materials containing Nb. The ratios have been determined for both annealed and reduced catalysts. As already reported, the ratios have been determined from the average amounts (weight %) of Nb and Ru detected by EDS in different regions of both annealed and reduced catalysts.

Overall, the Nb/Ru increases with increasing the Nb loading and it is shown that, among the annealed samples, 4Ru 2.5 Nb has the lowest Nb/Ru ratio, meaning that in this case the lowest amount of Nb is located at the surface and/or close to the surface of the material.

Upon reduction at 300 °C, an increased Nb/Ru ratio was observed for all the catalysts, which could be an indication that Nb migrates toward the surface of the catalyst under reducing conditions, possibly affecting the distribution of the highly dispersed Ru phase [42]. Moreover, such enhancement was minimum for 4Ru 2.5 Nb and it was particularly evident for 4Ru 7.5 Nb. These features corroborated that the Nb species are highly and homogeneously dispersed on the 4Ru 2.5 Nb material either after oxidation at 500 °C or after reduction at 300 °C, in agreement with XRD and FTIR-ATR results.

XPS analysis was made to gain further insight into the nature of Nb and Ru surface species and into their mutual interactions: in order to study the possible effect of Nb loading, the two samples with the lowest (4Ru 2.5 Nb) and highest (4Ru 7.5 Nb) Nb contents were examined, and reference has been made to the XPS study of the 4Ru0Nb sample reported elsewhere [24].

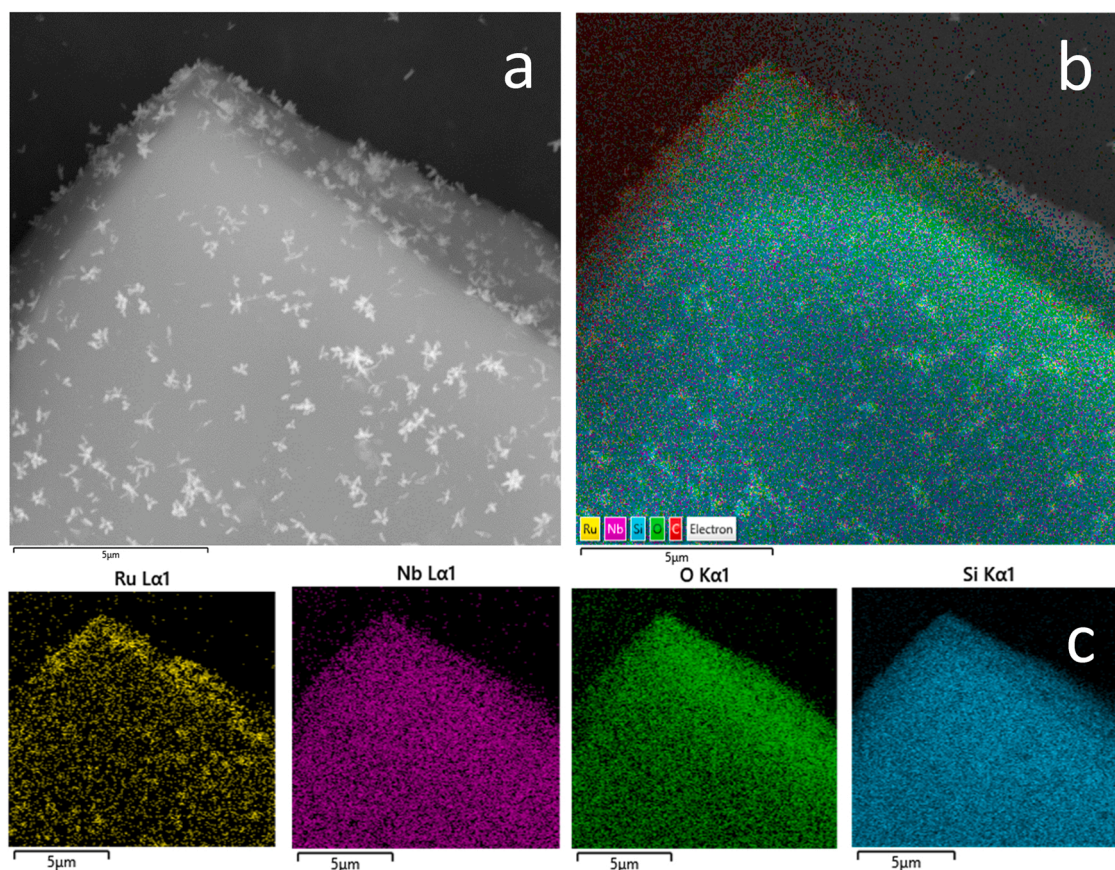By XPS, a Nb surface concentration of 1.0 and 2.1 at% was measured

Fig. 6. FESEM image of the 4Ru 7.5 Nb catalyst (a), EDS layered image (b) with the corresponding EDS maps of Ru, Nb, O, and Si (c). Image collected at 25 kV with the standard SE detector. Instrumental magnification: 15,000x.

with the 4Ru 2.5 Nb and the 4Ru 7.5 Nb samples, respectively, confirming the fact that, by the adopted synthesis procedure, Nb is not only at the surface, but also within the bulk, in agreement with the results obtained by ATR spectroscopy (Fig. S1), which clearly showed the formation of Nb—O—Si bonds and, thus, the incorporation of Nb in the silica matrix.

Fig. 7 shows the Nb 3d, O 1s and Ru 3d lines (panels a, b and c, respectively). As expected, the XP spectrum of Nb 3d shows a doublet: the Nb $3d_{5/2}$ line (Fig. 7a) is observed at 208.5 eV (4Ru 2.5 Nb) and at 208.1 eV (4Ru 7.5 Nb), both values being compatible with the occurrence of Nb^{5+} species. Interestingly, in bulk Nb_2O_5 the Nb $3d_{5/2}$ line is observed at 207.8 eV [43]: the higher BE value is assigned to a change in the coordination of Nb due to the formation of surface Nb—O—Si bonds, as already observed with other Nb_2O_5-SiO_2 materials obtained by impregnation [43], where, accordingly, the BE of the Nb $3d_{5/2}$ line was also observed to decrease at increasing Nb content. The result is a further confirmation of the occurrence of surface Nb species in a different environment than Nb_2O_5, and confirms the incorporation of Nb within the silica matrix. Correspondingly, the FWHM (Full Width at Half Maximum) of the Si 2p line (not shown) increases with the Nb content, as a result of a certain local disorder induced by the presence of Nb in the surroundings of surface Si atoms [43]: indeed, the FWHM of the Si 2p line, equal to 1.8 with the 4Ru0Nb sample [24], with Nb increased to 1.9 eV (4Ru 2.5 Nb) and 2.0 eV (4Ru 7.5 Nb).

The O 1s line (Fig. 7b) is characterized by three components occurring at 533.9, 533.1 and 530.9 eV with the 4Ru 2.5 Nb sample, and at 533.3, 533.1 and 531.1 eV with the 4Ru 7.5 Nb sample: the components are assigned to oxygen species of OH species (like adsorbed H_2O molecules), SiO_2 and RuO_2-like domains, respectively. With the 4Ru0Nb sample, three components were observed at 533.2 eV (H_2O), 532.9 eV (SiO_2) and 529.4 eV (RuO_2) [24]: interestingly, in the presence of Nb, all

the components shift to higher BE values, indicating, respectively, the effect of Nb on the acidic properties (in agreement with both TPD and IR spectroscopy results), on the environment of Si (in agreement with ATR results) and on Ru species (in agreement with FESEM and EDS mapping).

Fig. 7c reports the Ru 3d line region: as recognized in the literature, the overlapping of the C 1s and Ru $3d_{3/2}$ lines hampers an accurate analysis of the latter line, therefore only the Ru$3d_{5/2}$ line was analysed by the curve fitting (Fig. 7c) procedure previously adopted for the 4Ru0Nb sample [24], where the Ru 3d lines occurred at 280.2 (assigned to reduced Ru^0) and 280.6 eV (assigned to Ru^{4+} species). With the 4Ru 2.5 Nb sample, the two lines are observed at 280.3 (Ru^0) and 280.8 eV (Ru^{4+}), and with the 4Ru 7.5 Nb sample at 280.2 (Ru^0) and 280.7 eV (Ru^{4+}). As previously reported [24], the position of the line assigned to reduced Ru species is found at higher BE values with respect to some literature values [44]: as reported by Carrillo et al. [45], this can be due to the fact that the (at least partially) reduced Ru species are stabilized by a strong interaction with the SiO_2 support. As with the 4Ru0Nb sample, both Ru^0 and Ru^{4+} species were observed: the quantitative analysis showed that the percentage of reduced species (equal to 79 at% with the 4Ru0Nb sample, [24]) was ca. 41 and 37 at% with the 4Ru 2.5 Nb and the 4Ru 7.5 Nb sample, respectively. Indeed, with Ru nanoparticles supported on Nb-promoted boehmite [46], the surface Ru^{x+}/Ru^0 ratio was found to increase in the presence of Nb. As a whole, the here reported XPS data confirm the previous physico-chemical characterization and evidence a mutual Nb-Ru interaction in the studied samples.

In addition, the ruthenium dispersion in the reduced materials was also estimated by CO chemisorption and the results are summarized in Table 1. As established in our previous study [24], in the case of Ru catalysts synthesized by sol–gel this technique is a hardly applicable
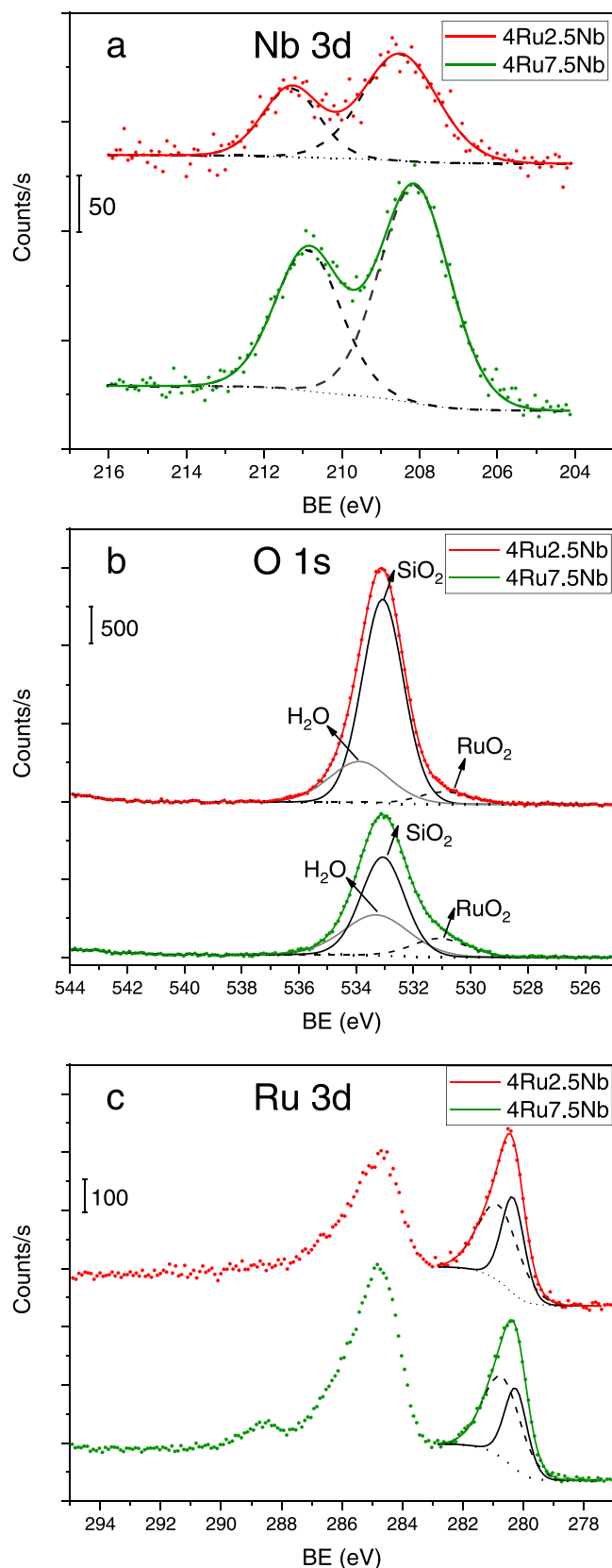
Fig. 7. XPS spectra of the 4Ru 2.5 Nb and the 4Ru 7.5 Nb samples: Nb 3d core level (a); O 1s core level (b) and Ru 3d core level (c).
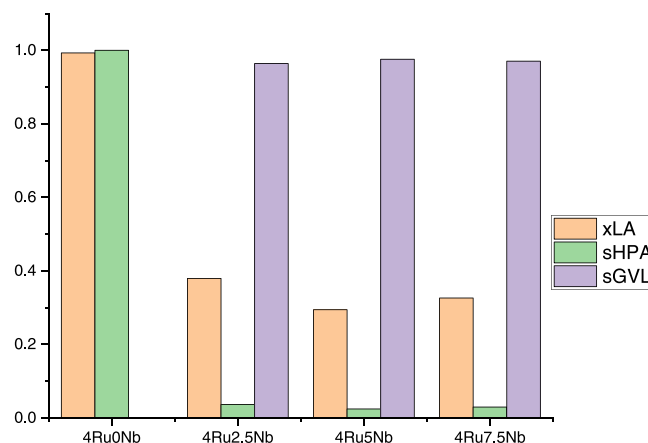

Fig. 8. Conversion (x) of LA and selectivity (s) to GVL and HPA obtained for each catalyst at 2 h reaction (70 °C, P_{H2}= 20 bar, 200 g water, 4.0 g LA, 0.5 g catalyst).

Table 2
TOF_{Ru}, TOF_{Ru}/D_{Ru} values and kinetic constants calculated on the experimental data.

Catalyst	TOF_{Ru} [s^{-1}]	TOF_{Ru}/D_{Ru} [s^{-1}]	k_1 [h^{-1}]	k_2 [h^{-1}]
4Ru0Nb	$(5.85 \pm 0.02) \cdot 10^{-2}$	$(4.9 \pm 0.2) \cdot 10^{-3}$	2.20 ± 0.04	0.010 ± 0.005
4Ru 2.5 Nb	$(1.24 \pm 0.02) \cdot 10^{-2}$	$(2.5 \pm 0.2) \cdot 10^{-3}$	0.26 ± 0.02	8.8 ± 0.1
4Ru5Nb	$(0.98 \pm 0.01) \cdot 10^{-2}$	$(2.0 \pm 0.2) \cdot 10^{-3}$	0.25 ± 0.02	29.4 ± 0.1
4Ru 7.5 Nb	$(0.95 \pm 0.01) \cdot 10^{-2}$	$(2.4 \pm 0.2) \cdot 10^{-3}$	0.25 ± 0.02	29.9 ± 0.2

method because it is difficult to exactly determine how many of the Ru atoms are incorporated into the three-dimensional network of the matrix covalent skeleton. Nevertheless, the Ru dispersion estimated for the 4Ru0Nb catalyst (about 12%) well agrees with the previously reported one [24]. The Nb addition gives an apparent lower dispersion (about 5%) that is the same independently from the Nb content. This result is related to the strong mutual interaction occurring between the Ru and Nb in agreement with the above characterization, that shows a similar elemental distribution among the studied catalysts [42,47].

In conclusion, the observed interaction between Nb and Ru is depending on the composition and affects both metal availability and acidity of the bifunctional Ru-Nb-Si catalysts.

3.4. Catalyst screening for LA hydrogenation to GVL

The Ru-Nb-Si catalysts were tested in the hydrogenation of LA to GVL, under mild conditions and in aqueous environment. In Fig. 8, the intermediate γ-hydroxypentanoic acid (HPA) and product (GVL) final concentrations (after 2 h) for each catalyst are displayed.

Using the 4Ru0Nb catalyst at the end of the reaction LA is completely converted into HPA and only traces of GVL were observed.

In the case of catalysts containing niobium the lactonization reaction of HPA to GVL was favored with almost complete selectivity to GVL whereas different final LA conversion values were obtained with the increase of niobium content indicating that the yield to GVL is strongly influenced by the acid characteristics of the matrix.

As demonstrated in our previous investigations, with dedicated experiments, the lactone is stable to hydrolysis when put in contact with the tested catalysts [20].

(1).

The turnover frequency (TOF) per mole of ruthenium was calculated

as the LA consumption rate referred to the number of moles of ruthenium, as shown in the following equation:

$$TOF_{Ru} = \frac{1}{n_{Ru}} \frac{dn_{LA}}{dt} \tag{1}$$

and the results obtained are shown in Table 2, where the TOF_{Ru} normalized with respect to the estimated dispersion values (TOF_{Ru}/D_{Ru}) are also displayed.

The TOF_{Ru} values calculated on the LA reveal the influence of catalyst composition on LA conversion. However, to investigate quantitatively the influence of morphology on both LA conversion and selectivity to GVL or HPA, deeper kinetic analysis of the data was performed.

The kinetic data collected using the different Ru-Nb-Si catalysts were elaborated using a pseudo-homogeneous kinetic model, which considers that the reaction is in series, the reagent LA produces the intermediate HPA in the first step, and HPA is converted into the product GVL in the second step:
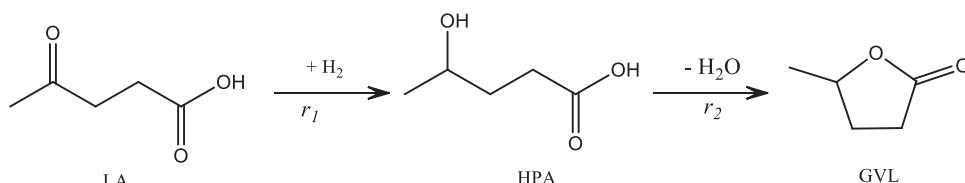
The rate of LA disappearance, r_1, is given by the equation:

$$r_1 = k_1 C_{LA} \tag{2}$$

The rate of disappearance of the intermediate HPA, r_2, is given by the equation:

$$r_2 = k_2 C_{HPA} \tag{3}$$

It is assumed that the kinetics are of the first order both in the first and in the second reaction step since the experiments were conducted in excess of hydrogen and both kinetic constants have physical dimensions equal to [h^{-1}]. The mass balance equations are as follows:

$$\frac{dC_{LA}}{dt} = -k_1 C_{LA} \tag{4}$$

$$\frac{dC_{HPA}}{dt} = +k_1 C_{LA} - k_2 C_{HPA} \tag{5}$$

$$\frac{dC_{GVL}}{dt} = + k_2 C_{HPA} \tag{6}$$

The two kinetic constants of the reactions, k_1 and k_2, were estimated and their values are displayed in Table 2.

In Fig. 9, as an example, the comparison between experimental data and the concentration profiles obtained by the model is displayed for 4Ru 2.5 Nb.

The values of k_1 calculated well agree with both TOF_{Ru} and TOF_{Ru}/D_{Ru} values (Table 2) pointing out that the hydrogenation is mainly controlled by extent of interaction between Ru and Nb: the presence of Nb lowering the reducibility of Ru, with a consequent lower amount of Ru^0 than Ru^{4+} (see previously reported XPS results) is responsible of the decrease of the hydrogenation activity. The lower Ru^0 concentration of samples containing Nb is also in agreement with the lower CO chemisorption values of these catalysts. Thus, the hydrogenation activity is maximum for the Nb-free catalyst (4Ru0Nb) and becomes lower with the presence of niobium, reaching a constant value. An opposite trend is seen for the lactonization kinetic constant k_2 that is mainly favored by

the increasing niobium content and so by the increasing of the acidity of the surface, determined with the surface analysis by FTIR spectroscopy (see Fig. 2).

It must be pointed out the observed 100% selectivity of 4Ru0Nb catalyst to HPA with the complete conversion of LA. At our knowledge this is the first case where such results have been reported.

The silica support for ruthenium in the LA hydrogenation is not extensively used because ruthenium catalysts on silica prepared by impregnation are subject to irreversible deactivation for the sintering phenomena [48]. However, in addition to the acidity of the support, selectivity can also be inflected by reaction conditions. For example, Kuwahara et al. [49], working at 70 °C (as in this work) with a ruthenium catalyst supported by impregnation on silica, achieved a selectivity of 4% at HPA for a conversion of 88% LA [49]. However, one must consider that in addition to the possible difference in acidity of the support, they used about 15 times higher concentration of LA and about 2.5 times higher concentration of catalyst. This certainly increases the acidity of the reaction environment.

Based on the above results, we explored the possibility to perform the whole transformation of LA to GVL by means of two separate and consecutive steps. In the former the LA hydrogenation to HPA takes place using the 4Ru0Nb catalyst and in the successive step the HPA dehydration to GVL occurs using a catalyst with suitable distribution of acid sites. For the latter step we used the 2.5 Nb$_2$O$_5$·97.5SiO$_2$ catalyst whose catalytic performance was described in a previous paper [26].

A preliminary test was performed adopting the same reaction conditions described in Section 2.3 for the first step, obtaining a liquid solution rich of HPA. This solution, in the consecutive step, was put in contact with the 2.5 Nb$_2$O$_5$·97.5SiO$_2$ catalyst, obtaining very encouraging results: after 2 h of reaction, HPA was fully converted in GVL, leading to no side product.
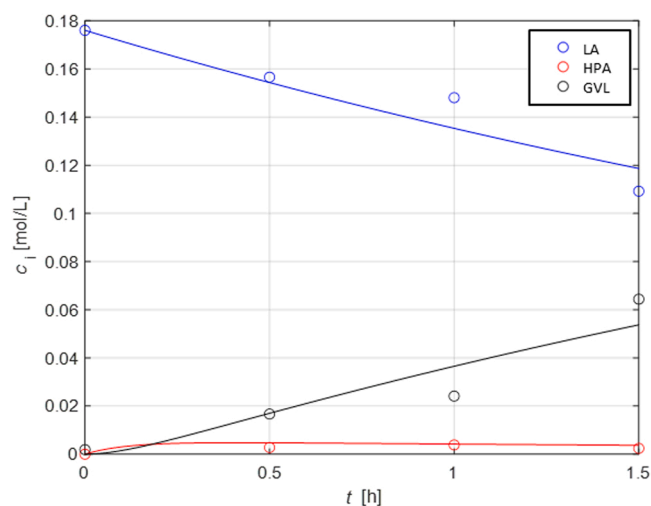

Fig. 9. Experimental data and calculated concentration profile for 4Ru 2.5 Nb as catalyst. (70 °C, P$_{H_2}$ = 20 bar, 200 g water, 4.0 g LA, 0.5 g catalyst).

4. Conclusions

Bifunctional ruthenium-niobium-silicon mixed oxides-based catalysts, with different contents of ruthenium and niobium, were studied for levulinic acid hydrogenation to γ-valerolactone. The results of catalytic tests in a fed-batch reactor under H_2 flow were coupled with a comprehensive characterization, in order to establish structure-activity relationships. The pre-reduced Ru-containing catalysts demonstrated to be effective in the hydrogenation of LA to HPA, whereas for the successive lactonization reaction the presence of niobium is necessary as it is responsible of the increased acidity of the catalyst. The sol-gel synthetic procedure allowed to obtain materials with high dispersion of both niobium and ruthenium and intimate interaction between them. Upon the reduction treatment, a competitive migration between the two metals takes place, leading to a variation in the surface exposure of Ru and Nb species. This phenomenon is strongly connected with the different Nb/Ru ratios of the catalysts and therefore affects in different extent the ruthenium availability, ultimately ruling the hydrogenation activity.

Furthermore, for the first time a catalyst has been found to obtain 100% selectivity to HPA at complete conversion of LA.

CRediT authorship contribution statement

All the authors have contributed to the design of experiments, the acquisition and analysis of the experimental data and the writing of the manuscript.

Declaration of Competing Interest

The authors declare that they have no known competing financial interests or personal relationships that could have appeared to influence the work reported in this paper.

Acknowledgments

Appendix A. Supplementary material

Supplementary data associated with this article can be found in the online version at doi:10.1016/j.apcatb.2022.121340.

References

[1] S.A. Razzak, M.M. Hossain, R.A. Lucky, A.S. Bassi, H. de Lasa, Integrated CO_2 capture, wastewater treatment and biofuel production by microalgae culturing—a review, Renew. Sustain. Energy Rev. 27 (2013) 622–653. ⟨https://econpapers.repec.org/RePEc:eee:rensus:v:27:y:2013:i:c:p:622-653⟩.

[2] T. Ansell, S. Cayzer, Limits to growth redux: a system dynamics model for assessing energy and climate change constraints to global growth, Energy Policy 120 (2018) 514–525, https://doi.org/10.1016/j.enpol.2018.05.053.

[3] T. Werpy, G. Petersen, Top Value Added Chemicals from Biomass Volume I, Us Nrel., Medium: ED; Size, 2004 p. 76. ⟨https://doi.org/10.2172/15008859⟩.

[4] Z. Xue, D. Yu, X. Zhao, T. Mu, Upgrading of levulinic acid into diverse N-containing functional chemicals, Green Chem. 21 (2019) 5449–5468, https://doi.org/10.1039/C9GC02415H.

[5] F.D. Pileidis, M.M. Titirici, Levulinic acid biorefineries: new challenges for efficient utilization of biomass, ChemSusChem 9 (2016) 562–582, https://doi.org/10.1002/cssc.201501405.

[6] J.J. Bozell, L. Moens, D.C. Elliott, Y. Wang, G.G. Neuenscwander, S.W. Fitzpatrick, R.J. Bilski, J.L. Jarnefeld, Production of levulinic acid and use as a platform chemical for derived products, Resour. Conserv. Recycl. 28 (2000) 227–239, https://doi.org/10.1016/S0921-3449(99)00047-6.

[7] M. Liu, S. Li, G. Fan, L. Yang, F. Li, Hierarchical flower-like bimetallic NiCu catalysts for catalytic transfer hydrogenation of ethyl levulinate into

γ-valerolactone, Ind. Eng. Chem. Res. 58 (2019) 10317–10327, https://doi.org/10.1021/acs.iecr.9b01774.

[8] K. Yan, Y. Yang, J. Chai, Y. Lu, Catalytic reactions of gamma-valerolactone: a platform to fuels and value-added chemicals, Appl. Catal. B Environ. 179 (2015) 292–304, https://doi.org/10.1016/j.apcatb.2015.04.030.

[9] D.M. Alonso, J.M.R. Gallo, M.A. Mellmer, S.G. Wettstein, J.A. Dumesic, Direct conversion of cellulose to levulinic acid and gamma-valerolactone using solid acid catalysts, Catal. Sci. Technol. 3 (2013) 927–931, https://doi.org/10.1039/c2cy20689g.

[10] M.G. Al-Shaal, A. Dzierbinski, R. Palkovits, Solvent-free γ-valerolactone hydrogenation to 2-methyltetrahydrofuran catalysed by Ru/C: a reaction network analysis, Green Chem. 16 (2014) 1358–1364, https://doi.org/10.1039/C3GC41803K.

[11] H. Wang, B. Yang, Q. Zhang, W. Zhu, Catalytic routes for the conversion of lignocellulosic biomass to aviation fuel range hydrocarbons, Renew. Sustain. Energy Rev. (2019), 109612, https://doi.org/10.1016/j.rser.2019.109612.

[12] I. Orlowski, M. Douthwaite, S. Iqbal, J.S. Hayward, T.E. Davies, J.K. Bartley, P. J. Miedziak, J. Hirayama, D.J. Morgan, D.J. Willock, G.J. Hutchings, The hydrogenation of levulinic acid to γ-valerolactone over Cu–ZrO2 catalysts prepared by a pH-gradient methodology, J. Energy Chem. 36 (2019) 15–24, https://doi.org/10.1016/j.jechem.2019.01.015.

[13] J. Wang, Y. Wang, X. Tong, Y. Wang, G. Jin, X. Guo, Highly active Ir/SiC catalyst for aqueous hydrogenation of levulinic acid to γ-valerolactone, Catal. Commun. 139 (2020), 105971, https://doi.org/10.1016/j.catcom.2020.105971.

[14] A.S. Amarasekara, M.A. Hasan, Pd/C catalyzed conversion of levulinic acid to γ-valerolactone using alcohol as a hydrogen donor under microwave conditions, Catal. Commun. 60 (2015) 5–7, https://doi.org/10.1016/j.catcom.2014.11.009.

[15] R.Y. Parapat, F.A. Yudatama, M.R. Musadi, M. Schwarze, R. Schomäcker, Antioxidant as structure directing agent in nanocatalyst preparation. Case study: catalytic activity of supported pt nanocatalyst in levulinic acid hydrogenation, Ind. Eng. Chem. Res. 58 (2019) 2460–2470, https://doi.org/10.1021/acs.iecr.8b03555.

[16] P.P. Upare, J.-M. Lee, D.W. Hwang, S.B. Halligudi, Y.K. Hwang, J.-S. Chang, Selective hydrogenation of levulinic acid to γ-valerolactone over carbon-supported noble metal catalysts, J. Ind. Eng. Chem. 17 (2011) 287–292, https://doi.org/10.1016/j.jiec.2011.02.025.

[17] A. Seretis, P. Diamantopoulou, I. Thanou, P. Tzevelekidis, C. Fakas, P. Lilas, G. Papadogianakis, Recent advances in ruthenium-catalyzed hydrogenation reactions of renewable biomass-derived levulinic acid in aqueous media, Front. Chem. 8 (2020) 221, https://doi.org/10.3389/fchem.2020.00221.

[18] L.E. Manzer, Catalytic synthesis of α-methylene-γ-valerolactone: a biomass-derived acrylic monomer, Appl. Catal. A Gen. 272 (2004) 249–256, https://doi.org/10.1016/j.apcata.2004.05.048.

[19] A.M.R. Galletti, C. Antonetti, V. De Luise, M. Martinelli, A sustainable process for the production of γ-valerolactone by hydrogenation of biomass-derived levulinic acid, Green Chem. 14 (2012) 688–694, https://doi.org/10.1039/c2gc15872h.

[20] L. Minieri, S. Esposito, V. Russo, B. Bonelli, D. Serio, B. Silvestri, A. Vergara, A. Aronne, A sol–gel ruthenium – niobium – silicon mixed-oxide bifunctional catalyst for the hydrogenation of levulinic acid in the aqueous phase, ChemCatChem 9 (2017) 1476–1486, https://doi.org/10.1002/cctc.201601547.

[21] Q. Yuan, H.H. van de Bovenkamp, Z. Zhang, A.S. Piskun, S. Sami, R.W.A. Havenith, H.J. Heeres, P.J. Deuss, Mechanistic investigations into the catalytic levulinic acid hydrogenation, insight in H/D exchange pathways, and a synthetic route to d 8-γ-valerolactone, ACS Catal. 11 (2021) 10467–10477, https://doi.org/10.1021/acscatal.1c02662.

[22] M. Jędrzejczyk, E. Soszka, J. Gosciancka, M. Kozanecki, J. Grams, A.M. Ruppert, The influence of carbon nature on the catalytic performance of Ru/C in levulinic acid hydrogenation with internal hydrogen source, Molecules 25 (2020), https://doi.org/10.3390/molecules25225362.

[23] Z. Yu, X. Lu, H. Bai, J. Xiong, W. Feng, N. Ji, Effects of solid acid supports on the bifunctional catalysis of levulinic acid to γ-valerolactone: catalytic activity and stability, Chem. Asian J. (2020) 1182–1201, https://doi.org/10.1002/asia.202000006.

[24] S. Esposito, B. Silvestri, V. Russo, B. Bonelli, M. Manzoli, F.A. Deorsola, A. Vergara, A. Aronne, M. Di Serio, Self-activating catalyst for glucose hydrogenation in the aqueous phase under mild conditions, ACS Catal. 9 (2019) 3426–3436, https://doi.org/10.1021/acscatal.8b04710.

[25] F. Murena, S. Esposito, F.A. Deorsola, C. Galletti, M.V. Prati, CO_2 abatement and CH4 recovery at vehicle exhausts: comparison and characterization of Ru powder and pellet catalysts, Int. J. Hydrog. Energy 45 (2020) 8640–8648, https://doi.org/10.1016/j.ijhydene.2020.01.120.

[26] R. Turco, A. Aronne, P. Carniti, A. Gervasini, L. Minieri, P. Pernice, R. Tesser, R. Vitiello, M. Di Serio, Influence of preparation methods and structure of niobium oxide-based catalysts in the epoxidation reaction, Catal. Today 254 (2015) 99–103, https://doi.org/10.1016/j.cattod.2014.11.033.

[27] P. Velmurugan, J. Shim, K.-J. Lee, M. Cho, S.-S. Lim, S.-K. Seo, K.-M. Cho, K.-S. Bang, B.-T. Oh, Extraction, characterization, and catalytic potential of amorphous silica from corn cobs by sol-gel method, J. Ind. Eng. Chem. 29 (2015) 298–303, https://doi.org/10.1016/j.jiec.2015.04.009.

[28] I. Rossetti, B. Bonelli, G. Ramis, E. Bahadori, R. Nasi, A. Aronne, S. Esposito, New insights into the role of the synthesis procedure on the performance of Co-based catalysts for ethanol steam reforming, Top. Catal. 61 (2018) 1734–1745, https://doi.org/10.1007/s11244-018-0969-3.

[29] A. Aronne, E. Marenna, V. Califano, E. Fanelli, P. Pernice, M. Trifuoggi, A. Vergara, Sol–gel synthesis and structural characterization of niobium-silicon mixed-oxide nanocomposites, J. Sol-Gel Sci. Technol. 43 (2007) 193–204, https://doi.org/10.1007/s10971-007-1563-5.

[30] A. Aronne, M. Turco, G. Bagnasco, P. Pernice, M. Di Serio, N.J. Clayden, E. Marenna, E. Fanelli, Synthesis of high surface area phosphosilicate glasses by a modified sol−gel method, Chem. Mater. 17 (2005) 2081–2090, https://doi.org/10.1021/cm047768t.

[31] M. Cerruti, G. Magnacca, V. Bolis, C. Morterra, Characterization of sol–gel bioglasses with the use of simple model systems: a surface-chemistry approach, J. Mater. Chem. 13 (2003) 1279–1286, https://doi.org/10.1039/B300961K.

[32] S. Esposito, A. Setaro, P. Maddalena, A. Aronne, P. Pernice, M. Laracca, Synthesis of cobalt doped silica thin film for low temperature optical gas sensor, J. Sol-Gel Sci. Technol. 60 (2011) 388–394, https://doi.org/10.1007/s10971-011-2483-y.

[33] P. Moggi, G. Predieri, F. Di Silvestri, A. Ferretti, Ru/SiO$_2$ catalysts prepared by the sol–gel method from Ru$_3$(CO)$_{12}$, Appl. Catal. A Gen. 182 (1999) 257–265, https://doi.org/10.1016/S0926-860X(99)00014-9.

[34] A. Aronne, M. Turco, G. Bagnasco, G. Ramis, E. Santacesaria, M. Di Serio, E. Marenna, M. Bevilacqua, C. Cammarano, E. Fanelli, Gel derived niobium-silicon mixed oxides: characterization and catalytic activity for cyclooctene epoxidation, Appl. Catal. A Gen. 347 (2008) 179–185, https://doi.org/10.1016/j.apcata.2008.06.011.

[35] N. Scotti, N. Ravasio, C. Evangelisti, R. Psaro, M. Penso, P.S. Niphadkar, V. V. Bokade, M. Guidotti, M, Epoxidation of Karanja (Millettia pinnata) oil methyl esters in the presence of hydrogen peroxide over a simple niobium-containing catalyst, Catalysts 9 (2019) 344, https://doi.org/10.3390/catal9040344.

[36] A. Gervasini, P. Carniti, F. Bossola, C. Imparato, P. Pernice, N.J. Clayden, A. Aronne, New Nb-P-Si ternary oxide materials and their use in heterogeneous acid catalysis, Mol. Catal., 458, pp. 280–286. ⟨https://doi.org/10.1016/j.mcat.2017.10.006⟩.

[37] B. Bonelli, I. Bottero, N. Ballarini, S. Passeri, F. Cavani, E. Garrone, IR spectroscopic and catalytic characterization of the acidity of imogolite-based systems, J. Catal. 264 (2009) 15–30, https://doi.org/10.1016/j.jcat.2009.03.003.

[38] A. Zecchina, S. Bordiga, G. Spoto, D. Scarano, G. Petrini, G. Leofanti, M. Padovan, C.O. Areàn, Low-temperature Fourier-transform infrared investigation of the interaction of CO with nanosized ZSM5 and silicalite, J. Chem. Soc. Faraday Trans. 88 (1992) 2959–2969, https://doi.org/10.1039/FT9928802959.

[39] B. Bonelli, M. Cozzolino, R. Tesser, M. Di Serio, M. Piumetti, E. Garrone, E. Santacesaria, Study of the surface acidity of TiO$_2$/SiO$_2$ catalysts by means of FTIR measurements of CO and NH3 adsorption, J. Catal. 246 (2007) 293–300, https://doi.org/10.1016/j.jcat.2006.12.015.

[40] A. Katovic, G. Giordano, B. Bonelli, B. Onida, E. Garrone, P. Lentz, J.B. Nagy, Preparation and characterization of mesoporous molecular sieves containing Al, Fe or Zn, Microporous Mesoporous Mater. 44–45 (2001) 275–281, https://doi.org/10.1016/S1387-1811(01)00193-7.

[41] B. Bonelli, B. Onida, J.D. Chen, A. Galarneau, F. Di Renzo, F. Fajula, E. Garrone, Spectroscopic characterisation of the strength and stability of the acidic sites of Al-rich microporous micelle-templated silicates, Microporous Mesoporous Mater. 67 (2004) 95–106, https://doi.org/10.1016/j.micromeso.2003.10.007.

[42] M.E. Grigorev, S.P. Mikhailov, A.V. Bykov, I.Y. Tiamina, L.Z. Nikoshvili, M. G. Sulman, A.L. Vasiliev, A.I. Sidorov, T.V. dos Santos, M.R. Meneghetti, S.M. P. Meneghetti, L.M. Bronstein, V.G. Matveeva, Surface interactions with the metal oxide surface control Ru nanoparticle formation and catalytic performance, Colloids Surf. A Physicochem. Eng. Asp. 610 (2021), 125722, https://doi.org/10.1016/j.colsurfa.2020.125722.

[43] S. Damyanova, L. Dimitrov, L. Petrov, P. Grange, Effect of niobium on the surface properties of Nb$_2$O$_5$-SiO$_2$-supported Mo catalysts, Appl. Surf. Sci. 214 (2003) 68–74, https://doi.org/10.1016/S0169-4332(03)00347-7.

[44] D.J. Morgan, Resolving ruthenium: XPS studies of common ruthenium materials, Surf. Interface Anal. 47 (2015) 1072–1079, https://doi.org/10.1002/sia.5852.

[45] A.I. Carrillo, L.C. Schmidt, M.L. Marín, J.C. Scaiano, Mild synthesis of mesoporous silica supported ruthenium nanoparticles as heterogeneous catalysts in oxidative Wittig coupling reactions, Catal. Sci. Technol. 4 (2014) 435–440, https://doi.org/10.1039/C3CY00773A.

[46] S. Jeon, Y.M. Park, J. Park, K. Saravanan, H.K. Jeong, J.W. Bae, Synergistic effects of Nb$_2$O$_5$ promoter on Ru/Al$_2$O$_3$ for an aqueous-phase hydrodeoxygenation of glycerol to hydrocarbons, Appl. Catal. A Gen. 551 (2018) 49–62, https://doi.org/10.1016/j.apcata.2017.12.006.

[47] W. Jiang, J.-P. Cao, X.-Y. Zhao, T. Xie, C. Zhu, J.-X. Xie, L. Zhao, M. Zhao, Y.-P. Zhao, J.-L. Zhang, Highly selective aromatic ring hydrogenation of lignin-derived compounds over macroporous Ru/Nb$_2$O$_5$ with the lost acidity at room temperature, Fuel 282 (2020) 118869, https://doi.org/10.1016/j.fuel.2020.118869.

[48] O.A. Abdelrahman, H.Y. Luo, A. Heyden, Y. Román-Leshkov, J.Q. Bond, Toward rational design of stable, supported metal catalysts for aqueous-phase processing: insights from the hydrogenation of levulinic acid, J. Catal. 329 (2015) 10–21, https://doi.org/10.1016/j.jcat.2015.04.026.

[49] Y. Kuwahara, Y. Magatani, H. Yamashita, Ru nanoparticles confined in Zr-containing spherical mesoporous silica containers for hydrogenation of levulinic acid and its esters into γ-valerolactone at ambient conditions, Catal. Today 258 (2015) 262–269, https://doi.org/10.1016/j.cattod.2015.01.015.